Numerical simulations for mixed convective hydromagnetic peristaltic flow in a curved channel with joule heating features

Raheel Ahmed, Nasir Ali, Sami Ullah Khan, et al.

ARTICLES YOU MAY BE INTERESTED IN

Heat and mass transfer together with hybrid nanofluid flow over a rotating disk
AIP Advances **10**, 055317 (2020); https://doi.org/10.1063/5.0010181

Unsteady peristaltic transport in curved channels
Physics of Fluids **25**, 091903 (2013); https://doi.org/10.1063/1.4821355

Numerical study at moderate Reynolds number of peristaltic flow of micropolar fluid through a porous-saturated channel in magnetic field
AIP Advances **8**, 015319 (2018); https://doi.org/10.1063/1.5019380
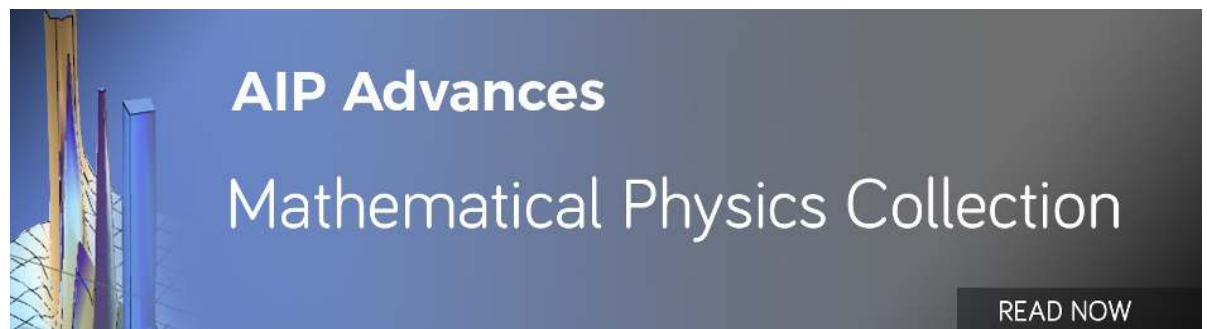
AIP Advances

Mathematical Physics Collection

READ NOW

10, 075303

Numerical simulations for mixed convective hydromagnetic peristaltic flow in a curved channel with joule heating features

View Online   Export Citation   CrossMark

Raheel Ahmed,[1]   Nasir Ali,[1]   Sami Ullah Khan,[2]   and   Iskander Tlili[3,4,a] (iD)

AFFILIATIONS

[1] Department of Mathematics and Statistics, International Islamic University, Islamabad 44000, Pakistan

[2] Department of Mathematics, COMSATS University Islamabad, Sahiwal 57000, Pakistan

[3] Institute of Research and Development, Duy Tan University, Da Nang 550000, Vietnam

[4] Faculty of Civil Engineering, Duy Tan University, Da Nang 550000, Vietnam

[a] Author to whom correspondence should be addressed: iskandertlili@duytan.edu.vn

ABSTRACT

This article investigates the flow and mass transportation characteristics in the peristaltic motion configured by a heated curved channel. The coupling between momentum and energy equation is achieved using the Boussinesq approximation. The equations describing the flow and heat/mass transfer are developed using curvilinear coordinates. A reduction of these equations is made based on the lubrication approximation. The reduced linear ordinary differential equations are integrated numerically using an implicit finite difference scheme. The effects of thermal and concentration Grashof numbers, Hartmann number, Brinkmann number, and curvature parameter on longitudinal velocity, pressure rise, temperature, and mass concentration are analyzed in detail. It is found that the temperature field is enhanced with an increase in the thermal Grashof number and Hartmann number, while the mass concentration decreases with an increase in the thermal Grashof number and Hartmann number. The flow patterns in the channel illustrating the effects of Grashof numbers, Brinkmann number, and Hartmann number are also displayed. It is observed that flow movements become intense for greater values of Brinkman number, thermal Grashof number, and Hartmann number.

I. INTRODUCTION

The flow problems related to the mixed convection flows encountered valuable applications in engineering and industrial areas. The mixed convection is associated with the collective features of forced convection and natural convection in the heat transportation process. The most glowing demonstration of this mixed convection is the movement of the temperature stratified mass of water and air prospective of Earth, which are comprehensively investigated in the geophysics. In many engineering devices, the role of the mixed convection cannot be denied at the micro-scale level. The heat transfer process in human brain, liver, and skeletal muscle contraction includes the application of this interesting phenomenon. The important phenomena of mixed convection are extensively studied in the context of the boundary layer and peristaltic flows. We shall first present a brief review of the recent literature on mixed convective boundary layer flows and then turn back to important recent literature on mixed convective peristaltic flows. Ramachandran et al.[1] utilized the influence of mixed convection features in the stagnation point study of the moving heated surface for which the wall temperature and the surface heat flux were assumed to be of a variable nature. Chamkha et al.[2] studied the effects of mixed convection on unsteady flow over a stretching surface. Lok et al.[3] analyzed two-dimensional steady flow of micropolar fluid in the presence of mixed convection features configured by a vertical surface. The proposed flow model is based on the consideration of the stagnation point and uniform shear flow that are taken parallel to the stretched surface. The investigation that deals with the slip flow of viscous fluid

also featuring mixed convection consequences was reported by Rohni *et al.*[4] Lok *et al.*[5] worked on the non-orthogonal stagnation point mixed convective flow of micropolar liquid confined by a vertical geometry. Prasad *et al.*[6] investigated mixed convective flow of fluid with variable properties over a non-linear stretching surface. The utilization of slip characteristics in convective flow induced due to the heated flat surface was worked out by Bhattacharyya *et al.*[7] The mixed convection prospective of the nanomaterial through a porous space has been pointed out by Rana *et al.*[8] Rosali *et al.*[9] also pointed out the importance of mixed convection due to the porous cone with the utilization of convective wall constants. Vajravelu *et al.*[10] presented a comprehensive study on mixed convection with heat and mass transfer of Ostwald-de Waele fluid over a vertical stretching sheet. Some dual solutions based on a numerical algorithm regarding a mixed convection flow problem have been successfully targeted by Ishak *et al.*[11] Abbas *et al.*[12] examined the mixed convective stagnation-point flow of a Maxwell fluid toward a vertical stretching surface. Jamaludin *et al.*[13] examined a three-dimensional mixed convection stagnation-point flow over a permeable vertical surface. The thermally saturated and mixed convective flow of viscous fluid with the interesting features of viscous dissipation and Joule heating through a porous stretched surface was numerically investigated by Chen.[14] Turkyilmazoglu[15] studied mixed convective heat transfer over a permeable stretching surface analytically with magnetohydrodynamic effects. Aydin and Kaya[16] examined mixed convective viscous flow over a vertical flat plate. The mixed convection features regarding the investigation of stagnation point flow encountered by a lubricated surface was numerically explored by Mahmood *et al.*[17] Bhatti *et al.*[18] examined the mixed convection aspects in blood flow of nanoparticles containing gyrotactic microorganisms through tapered arteries. Zhang *et al.*[19] investigated mixed convection flow of nanofluid with gyrotactic microorganisms encountered by rotating circular plates.

The flow induced due to sinusoidally deformed vessel walls is commonly known as peristaltic flow. Peristaltic flows are caused by rythmic contractions and relaxations of smooth muscles of the vessel. Peristalsis is a major mechanism found in the human body for physiological fluid transport. Examples of physiological fluids transported by peristaltic activity are spermatic fluid, chyme, blood, and urine. Modern machines which operate on the principle of peristalsis are roller and finger pumps, diabetic pumps, pharmacological delivery systems, heart-lung machine, etc. Eldabe *et al.*[20] involved temperature dependent viscosity consequences of the peristaltic movement of viscoelastic fluid. The mixed convection characteristics in the peristaltic motion of viscous fluid confined by an asymmetric channel have been observed by Srinivas *et al.*[21] Another useful theoretical contribution performed by Srinivas and Muthuraj[22] concerned with peristaltic flow in an asymmetric channel under the additional influence of a chemical reaction and porous space. The mixed convection aspects in peristaltic flow controlled by slip constraints is reported by Noreen *et al.*[23] Shehzad *et al.*[24] highlighted the thermophoretic aspects in the peristaltic pattern of nanoparticles with mixed convection feature. The peristaltic flow procedure in the inclined channel filled by the nanoparticles with the impact of wall slip has been surveyed by Abbasi *et al.*[25] Tanveer *et al.*[26] discussed shear-thinning and shear-thickening effects in mixed convective peristaltic flow of Sisko fluid. The peristaltic motion for the convective flow of magnetized Carreau fluid assumed in a curved channel was scrutinized by Hayat *et al.*[27] In another attempt, Hayat *et al.*[28] introduced variable properties for the peristaltic flow phenomenon with the external features of a magnetic field. The heat transfer characteristics in peristaltic flow of viscous fluid in the presence of Hall current features was investigated by Bhatti *et al.*[29] Other investigations on this topic may be found in Refs. 30–34.

The existing literature surveyed by the author deals with non-isothermal peristaltic flows of different non-Newtonian fluids in the planar channel, axisymmetric tube, curved channel, or a rectangular duct. However, less attention is given to the simultaneous effects of heat and mass transfer in peristaltic flow through the curved geometry. The purpose of the present research is to investigate the peristaltic flow with heat and mass transfer in a curved channel through the use of different non-Newtonian fluid models. Motivated by this fact, the research carried out in this thesis provides the improvement of existing mathematical models of the peristaltic transport of Newtonian and generalized Newtonian fluids, interpretation of the fundamental equations, and examination of different key factors on flow and heat/mass transfer features.

From the literature cited above, it has been visualized that the mixed convective peristaltic flow through a curved channel is studied but less attention is paid to mixed convective heat and mass transfer in hydromagnetic peristaltic flow through a curved channel with the Joule heating effect. Therefore, the prime objective of this study is to investigate the effects of Grashof number, Hartmann number, Brinkmann number, and dimensionless radius of curvature on flow, heat, and mass transfer characteristics. It is remarked that no such investigation in flow through the curved channel has been presented in the literature and, subsequently, this investigation aims to fill this gap. The current investigation deals with peristaltic pumping that encountered interesting medical instrument applications like blood pump and heart lung devices. Some more fundamental applications associated with the current work involve the transport of urine from kidney to bladder via the ureter, ovum movement associated with the fallopian tube, food swallowing in the esophagus, circulation of blood in blood vessels, etc.

To this end, the governing equations for velocity, temperature, and mass concentration are modeled. The modeled system is solved numerically with the help of the finite difference scheme. The fluid velocity, temperature, and concentration fields are analyzed for several values of involved parameters.

II. FLOW MODEL

In order to develop the governing equations for peristaltic flow problem, we assume a curved channel having width $2w$ coiled circularly, which have center O and radius R_0, as illustrated in Fig. 1. It is assumed that the curved channel is filled with homogeneous fluid for which flow is incompressible. The flow has been induced due to the sinusoidal deformation of the walls of the channel. The magnetic field is imposed in the radial direction. Let c and a represent, respectively, the waves propagating and amplitude in channel boundaries. The upper wall of the channel is driven at a constant temperature T_0, while the lower surface of the channel is confined to temperature T_1.
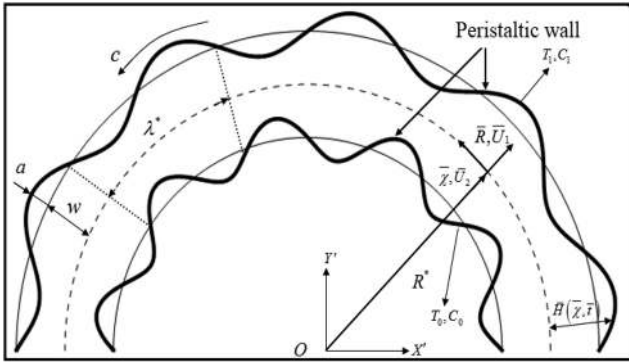
FIG. 1. Geometry of the problem.

The whole flow system is modeled in a curvilinear coordinate system (R, χ, Z), where R is suggested in the radial direction, χ has been assumed in the direction of fluid flow, while Z is taken perpendicular to the plane confined by R and χ.

The shape of both walls is described mathematically as

$$H_1(\chi, t) = w + a \sin\left(\left(\frac{2\pi}{\lambda^*}\right)(\chi - ct)\right), \quad \text{Upper wall,} \quad (1)$$

$$H_2(\chi, t) = -w - a \sin\left(\left(\frac{2\pi}{\lambda^*}\right)(\chi - ct)\right), \quad \text{Lower wall,} \quad (2)$$

where λ^* is the wavelength and t is the time. We use the following associated equations to model the current flow problem:

$$\nabla \cdot \mathbf{U} = 0, \quad (3)$$

$$\rho \frac{d\mathbf{U}}{dt} = \nabla \cdot \boldsymbol{\tau} - \rho \vec{g} \beta (T - T_0) - \rho \vec{g} \beta (C - C_0) + \mathbf{J} \times \mathbf{B}, \quad (4)$$

$$\rho c_p \frac{dT}{dt} = k \nabla^2 T + \mu \Phi + \frac{\sigma B_0^2 \tilde{R}^2}{(R + \tilde{R})^2} U^2, \quad (5)$$

$$\frac{dC}{dt} = D \nabla^2 C + \frac{D K_T}{T_m} \nabla^2 T. \quad (6)$$

Some physical variables in above equations $\boldsymbol{\tau}$, $\mathbf{U}$, T, c_p, μ, k, $\sigma\Phi$, and ρ indicate the Cauchy stress tensor, velocity, temperature, specific heat constant, viscosity, thermal conductivity, dissipation function, Stefan–Boltzman constant, and fluid density, respectively.

The radial magnetic field $\mathbf{B}$ is given by

$$\mathbf{B} = \left(\frac{B^* \tilde{R}}{R + \tilde{R}}\right) e_R, \quad (7)$$

where B^* is the characteristic magnetic induction in the limit $\tilde{R} \to \infty$ and e_R is the unit vector in the radial direction. It is pointed out here that the magnetic field given by Eq. (7) is solenoidal and satisfies Maxwell's equations.

Using Eq. (7), the term $\mathbf{J} \times \mathbf{B}$ in Eq. (4) is given by

$$\mathbf{J} \times \mathbf{B} = -\left(\frac{\sigma B^{*2} U_2 \tilde{R}^2}{(R + \tilde{R})^2}\right) e_X, \quad (8)$$

where e_X denotes the azimuthal direction unit vector.

Assuming $\mathbf{U} = [U_1(\chi, R, t), U_2(\chi, R, t), 0]$, and $T = T(\chi, R, t)$, Eqs. (3)–(6) yield

$$\tilde{R}\left(\frac{\partial U_2}{\partial \chi}\right) + \frac{\partial}{\partial R}\left\{(R + \tilde{R}) U_1\right\} = 0, \quad (9)$$

$$\frac{\partial U_1}{\partial t} + U_1 \frac{\partial U_1}{\partial R} + \frac{R U_2}{R + \tilde{R}} \frac{\partial U_1}{\partial \chi} - \frac{U_2^2}{R + \tilde{R}}$$
$$= -\frac{1}{\rho} \frac{\partial P}{\partial R} + \nu \left[\frac{1}{R + \tilde{R}} \frac{\partial}{\partial R} \left\{(R + \tilde{R}) \frac{\partial U_1}{\partial R}\right\} + \left(\frac{\tilde{R}}{R + \tilde{R}}\right)^2 \frac{\partial^2 U_1}{\partial \chi^2} \right.$$
$$\left. - \frac{U_1}{(R + \tilde{R})^2} - \frac{2\tilde{R}}{(R + \tilde{R})^2} \frac{\partial U_2}{\partial \chi} \right], \quad (10)$$

$$\frac{\partial U_2}{\partial t} + U_1 \frac{\partial U_2}{\partial R} + \frac{\tilde{R} U_2}{R + \tilde{R}} \frac{\partial U_2}{\partial \chi} + \frac{U_2 U_1}{R + \tilde{R}}$$
$$= -\frac{\tilde{R}}{\rho(R + \tilde{R})} \frac{\partial P}{\partial \chi} + \nu \left[\frac{1}{(R + \tilde{R})} \frac{\partial}{\partial R} \left\{(R + \tilde{R}) \frac{\partial U_2}{\partial R}\right\} \right.$$
$$\left. + \left(\frac{\tilde{R}}{R + \tilde{R}}\right)^2 \frac{\partial^2 U_2}{\partial \chi^2} - \frac{U_2}{(R + \tilde{R})^2} + \frac{2\tilde{R}}{(R + \tilde{R})^2} \frac{\partial U_1}{\partial \chi} \right]$$
$$- \rho \vec{g} \beta (T - T_0) - \rho \vec{g} \beta (C - C_0) - \frac{\sigma B^{*2} \tilde{R}^2 U_2}{(R + \tilde{R})^2}, \quad (11)$$

$$\rho c_p \left[\frac{\partial T}{\partial t} + U_1 \frac{\partial T}{\partial R} + \frac{\tilde{R} U_2}{R + \tilde{R}} \frac{\partial T}{\partial \chi} \right]$$
$$= k \left(\frac{1}{(R + \tilde{R})} \frac{\partial}{\partial R} \left\{(R + \tilde{R}) \frac{\partial T}{\partial R}\right\} + \left(\frac{\tilde{R}}{R + \tilde{R}}\right)^2 \frac{\partial^2 T}{\partial \chi^2} + \mu \left[2\left(\frac{\partial U_1}{\partial R}\right)^2 \right. \right.$$
$$+ \left(\frac{\tilde{R}}{R + \tilde{R}} \frac{\partial U_1}{\partial \chi} - \frac{U_2}{R + \tilde{R}}\right)\left(\frac{\partial U_2}{\partial R} + \frac{\tilde{R}}{R + \tilde{R}} \frac{\partial U_1}{\partial \chi} - \frac{U_2}{R + \tilde{R}}\right)$$
$$+ \frac{\partial U_2}{\partial R}\left(\frac{\partial U_2}{\partial R} + \frac{\tilde{R}}{R + \tilde{R}} \frac{\partial U_1}{\partial \chi} - \frac{U_2}{R + \tilde{R}}\right)$$
$$\left. \left. + 2\left(\frac{\tilde{R}}{R + \tilde{R}} \frac{\partial U_2}{\partial \chi} + \frac{U_1}{R + \tilde{R}}\right) \right] + \frac{\sigma B^{*2} \tilde{R}^2}{(R + \tilde{R})^2} U_2^2, \quad (12)$$

$$\left[\frac{\partial}{\partial t} + U_1 \frac{\partial}{\partial R} + \frac{\tilde{R} U_2}{R + \tilde{R}} \frac{\partial}{\partial X} \right] C$$
$$= D \left(\frac{\partial^2}{\partial R^2} + \frac{\tilde{R}}{R + \tilde{R}} \frac{\partial}{\partial R} + \left(\frac{\tilde{R}}{R + \tilde{R}}\right)^2 \frac{\partial^2}{\partial X^2} \right) C$$
$$+ \frac{D K_T}{T_m} \left(\frac{\partial^2 T}{\partial R^2} + \frac{\tilde{R}}{R + \tilde{R}} \frac{\partial T}{\partial R} + \left(\frac{\tilde{R}}{R + \tilde{R}}\right)^2 \frac{\partial^2 T}{\partial X^2} \right). \quad (13)$$

The boundary conditions associated with Eqs. (9)–(13) are

$$U_2 = 0, \ U_1 = \frac{\partial H_1}{\partial t}, \ T = T_0, \ C = C_0, \text{ at } R = H_1(\chi, t), \quad (14)$$

$$U_2 = 0, \ U_1 = \frac{\partial H_2}{\partial t}, \ T = T_1, \ C = C_1, \text{ at } R = H_2(\chi, t). \quad (15)$$

The following transformations are used to convert the problem from the fixed frame (R, χ) to the new wave frame (r, x):

$$x = \chi - ct,\ r = R,\ p = P,\ u_1 = U_1,\ u_2 = U_2 - c,\ T = T. \quad (16)$$

Substituting the above quantities, we obtained the following set of flow equations in the wave frame:

$$\frac{\partial}{\partial r}\left\{(r + \tilde{R})u_1\right\} + \tilde{R}\frac{\partial u_2}{\partial x} = 0, \quad (17)$$

$$-c\frac{\partial u_1}{\partial x} + u_1\frac{\partial u_1}{\partial r} + \frac{\tilde{R}(u_2 + c)}{r + \tilde{R}}\frac{\partial u_1}{\partial x} - \frac{(u_2 + c)^2}{r + \tilde{R}}$$
$$= -\frac{1}{\rho}\frac{\partial P}{\partial r} + v\left[\frac{1}{r + \tilde{R}}\frac{\partial}{\partial r}\left\{(r + \tilde{R})\frac{\partial u_1}{\partial r}\right\}\right.$$
$$\left. + \left(\frac{\tilde{R}}{r + \tilde{R}}\right)^2\frac{\partial^2 u_1}{\partial x^2} - \frac{u_1}{(r + \tilde{R})^2} - \frac{2\tilde{R}}{(r + \tilde{R})^2}\frac{\partial u_2}{\partial x}\right], \quad (18)$$

$$-c\frac{\partial u_2}{\partial x} + u_1\frac{\partial u_2}{\partial r} + \frac{\tilde{R}(u_2 + c)}{r + \tilde{R}}\frac{\partial u_2}{\partial x} - \frac{(u_2 + c)u_1}{r + \tilde{R}}$$
$$= -\frac{\tilde{R}}{\rho(r + \tilde{R})}\frac{\partial P}{\partial x} + v\left[\frac{1}{(r + \tilde{R})}\frac{\partial}{\partial r}\left\{(r + \tilde{R})\frac{\partial u_2}{\partial r}\right\}\right.$$
$$\left. + \left(\frac{\tilde{R}}{r + \tilde{R}}\right)^2\frac{\partial^2 u_2}{\partial x^2} - \frac{u_2}{(r + \tilde{R})^2} + \frac{2\tilde{R}}{(r + \tilde{R})^2}\frac{\partial u_1}{\partial x}\right]$$
$$- \rho\vec{g}\beta(T - T_0) - \rho\vec{g}\beta(C - C_0) - \frac{\sigma B^{*2}\tilde{R}^2(u_2 + c)}{(r + \tilde{R})^2}, \quad (19)$$

$$\rho c_p\left[-c\frac{\partial T}{\partial x} + u_1\frac{\partial T}{\partial r} + \frac{\tilde{R}(u_2 + c)}{r + \tilde{R}}\frac{\partial T}{\partial x}\right]$$

$$= k\left(\frac{1}{(r + \tilde{R})}\frac{\partial}{\partial r}\left\{(r + \tilde{R})\frac{\partial T}{\partial r}\right\} + \left(\frac{\tilde{R}}{r + \tilde{R}}\right)^2\frac{\partial^2 T}{\partial x^2}\right) + \mu\left[2\left(\frac{\partial u_1}{\partial r}\right)^2\right.$$

$$+ \left(\frac{\tilde{R}}{r + \tilde{R}}\frac{\partial u_1}{\partial x} - \frac{(u_2 + c)}{r + \tilde{R}}\right)\left(\frac{\partial u_2}{\partial r} + \frac{\tilde{R}}{r + \tilde{R}}\frac{\partial u_1}{\partial x} - \frac{(u_2 + c)}{r + \tilde{R}}\right)$$

$$+ \frac{\partial u_2}{\partial r}\left(\frac{\partial u_2}{\partial r} + \frac{\tilde{R}}{r + \tilde{R}}\frac{\partial u_1}{\partial x} - \frac{(u_2 + c)}{r + \tilde{R}}\right)$$

$$\left. + 2\left(\frac{\tilde{R}}{r + \tilde{R}}\frac{\partial u_2}{\partial x} + \frac{u_1}{r + \tilde{R}}\right)\right] + \frac{\sigma B^{*2}\tilde{R}^2}{(r + \tilde{R})^2}(u_2 + c)^2, \quad (20)$$

$$\text{Re}\left[\delta\frac{\partial\phi}{\partial x} + u_1\frac{\partial\phi}{\partial\eta} + \frac{\delta k(u_2 + 1)}{\eta + k}\frac{\partial\phi}{\partial x}\right]$$

$$= \frac{1}{Sc}\left(\frac{\partial^2\phi}{\partial\eta^2} + \frac{1}{\eta + k}\frac{\partial\phi}{\partial\eta} + \delta^2\left(\frac{k}{\eta + k}\right)^2\frac{\partial^2\phi}{\partial x^2}\right)$$

$$+ Sr\left(\frac{\partial^2\phi}{\partial\eta^2} + \frac{1}{\eta + k}\frac{\partial\phi}{\partial\eta} + \delta^2\left(\frac{k}{\eta + k}\right)^2\frac{\partial^2\phi}{\partial x^2}\right). \quad (21)$$

The following dimensionless variables are defined to render the above equations in the normalized form:

$$\tilde{x} = \frac{2\pi}{\lambda^*}x,\ \eta = \frac{r}{a_1},\ \bar{u}_1 = \frac{u_1}{c_1},\ \bar{u}_2 = \frac{u_2}{c_1},\ \bar{p} = \frac{2\pi a_1^2}{\lambda^*\mu c}p,\ \delta = \frac{2\pi a_1}{\lambda^*},\ \text{Re} = \frac{\rho c a_1}{\mu},\ Ha = a_1 B^*\sqrt{\frac{\sigma}{\mu}},$$
$$\gamma = \frac{\tilde{R}}{a_1},\ \theta = \frac{T - T_1}{T_0 - T_1},\ \phi = \frac{C - C_1}{C_0 - C_1},\ Br = \frac{\mu c^2}{k(T_0 - T_1)},\ Gr_C = \frac{a^2\rho\vec{g}\beta(C - C_0)}{\mu c},\ Gr_T = \frac{a^3\vec{g}\beta(T_0 - T_1)}{v^2}. \quad (22)$$

In above equations, Re, δ, γ, and K^* represent the Reynolds number, the wave number, and the dimensionless radius of curvature, respectively.

In view of dimensionless parameters defined in Eq. (22), we further suggest the following stream functions:

$$u_1 = \delta\frac{\gamma}{\eta + \gamma}\frac{\partial\psi}{\partial x},\ u_2 = -\frac{\partial\psi}{\partial\eta}. \quad (23)$$

Equation (17) is identically satisfied and Eqs. (18)–(21) after employing long wavelength and low Reynolds approximations contract to

$$\frac{\partial p}{\partial\eta} = 0, \quad (24)$$

$$-\frac{\partial p}{\partial x} - \frac{1}{\gamma}\left(\frac{\partial}{\partial\eta}\left\{(\eta + \gamma)\frac{\partial^2\psi}{\partial\eta^2}\right\} + \frac{1}{\eta + \gamma}\left(1 - \frac{\partial\psi}{\partial\eta}\right)\right)$$

$$+ \frac{Gr_T\theta(\eta + \gamma)}{\text{Re}\,\gamma} + \frac{Gr_C\phi(\eta + \gamma)}{\text{Re}\,\gamma} - \frac{\gamma Ha^2}{\eta + \gamma}\left(1 - \frac{\partial\psi}{\partial\eta}\right) = 0, \quad (25)$$

$$\frac{\partial^2\theta}{\partial\eta^2} + \frac{1}{(\eta + \gamma)}\frac{\partial\theta}{\partial\eta} + Br\left(-\frac{1}{\eta + \gamma}\left(1 - \frac{\partial\psi}{\partial\eta}\right) - \frac{\partial^2\psi}{\partial\eta^2}\right)^2$$

$$+ \frac{BrHa^2\gamma^2}{(\eta + \gamma)^2}\left(1 - \frac{\partial\psi}{\partial\eta}\right)^2 = 0, \quad (26)$$

$$\frac{1}{Sc}\left(\frac{\partial^2\phi}{\partial\eta^2} + \frac{1}{(k + \eta)}\frac{\partial\phi}{\partial\eta}\right) + Sr\left(\frac{\partial^2\theta}{\partial\eta^2} + \frac{1}{(k + \eta)}\frac{\partial\theta}{\partial\eta}\right) = 0. \quad (27)$$

After eliminating the pressure from Eqs. (24) and (25), we obtained the following associated differential equation:

$$\frac{\partial}{\partial \eta}\left[\frac{1}{\gamma}\left(\frac{\partial}{\partial \eta}\left\{(\eta + \gamma)\frac{\partial^2 \psi}{\partial \eta^2}\right\} + \frac{1}{\eta + \gamma}\left(1 - \frac{\partial \psi}{\partial \eta}\right)\right) - \frac{Gr_T \theta(\eta + \gamma)}{\mathrm{Re}\, \gamma}\right.$$
$$\left. + \frac{\phi Gr_C(\eta + k)}{k} + \frac{\gamma Ha^2}{\eta + \gamma}\left(1 - \frac{\partial \psi}{\partial \eta}\right)\right]. \qquad (28)$$

Similarly, the constituted boundary conditions for the formulated flow problem are

$$\psi = -\frac{q}{2}, \ \frac{\partial \psi}{\partial \eta} = 1, \ \theta = 0, \ \phi = 0, \ \text{at } \eta = h_1 = 1 + \lambda \sin x, \quad (29)$$

$$\psi = \frac{q}{2}, \ \frac{\partial \psi}{\partial \eta} = 1, \ \theta = 1, \ \phi = 1, \ \text{at } \eta = h_2 = -1 - \lambda \sin x, \quad (30)$$

where $\lambda = a/w$ symbolized the amplitude ratio. Now, we aim to simulate the solution of Eqs. (26)–(28) with the help of boundary assumptions (29) and (30). Now, we make relations for the pressure rise per wavelength (Δp), the coefficient of heat transfer $z_i(i = 1, 2)$, and Sherwood number $Sh_i(i = 1, 2)$ at upper and lower surfaces as follows:

$$\Delta p = \int_0^{2\pi} \frac{dp}{dx} dx, \qquad (31)$$

$$z = \frac{\partial h_i}{\partial x}\frac{\partial \theta}{\partial \eta}\bigg|_{\eta = h_i}, \quad i = 1, 2. \qquad (32)$$

$$Sh = \frac{\partial h_i}{\partial x}\frac{\partial \phi}{\partial \eta}\bigg|_{\eta = h_i}, \quad i = 1, 2. \qquad (33)$$

III. FINITE DIFFERENCE SCHEME

Although Eqs. (26)–(28) are linear ordinary differential equations, their closed form solutions are difficult to obtain. Therefore, these transmuted equations are numerically treated by following the numerical procedure. For this, we employ the implicit finite difference technique to obtain numerical results. In this technique, the original flow equations are transmuted into a linear one at the $(m + 1)$th iterative step. We employ the following iterative procedure to start the numerical computations:

$$\frac{\partial^4 \psi^{(m+1)}}{\partial \eta^4} + \frac{2\partial^3 \psi^{(m+1)}}{(\eta + \gamma)\partial \eta^3} - \left\{\frac{1}{(\eta + \gamma)^2} + \frac{\gamma^2 Ha^2}{(\eta + \gamma)^2}\right\}\frac{\partial^2 \psi^{(m+1)}}{\partial \eta^2}$$
$$+ \left\{-\frac{1}{(\eta + \gamma)^3} + \frac{\gamma^2 Ha^2}{(\eta + \gamma)^3}\right\}\frac{\partial \psi^{(m+1)}}{\partial \eta}$$
$$- \frac{Gr_T \theta}{\mathrm{Re}(\eta + \gamma)} + \frac{Gr_C \phi}{\mathrm{Re}(\eta + \gamma)} - \frac{1}{(\eta + \gamma)^3} - \frac{\gamma^2 Ha^2}{(\eta + \gamma)^3} = 0, \quad (34)$$

$$\frac{\partial^2 \theta^{(m+1)}}{\partial \eta^2} + \frac{1}{\gamma + \eta}\frac{\partial \theta^{(m+1)}}{\partial \eta} = -Br\left(-\frac{1}{\gamma + \eta}\left(1 - \frac{\partial \psi^{(m)}}{\partial \eta}\right) - \frac{\partial^2 \psi^{(m)}}{\partial \eta^2}\right)^2$$
$$- \frac{BrHa^2 \gamma^2}{(\gamma + \eta)^2}\left(1 - \frac{\partial \psi^{(m)}}{\partial \eta}\right)^2, \qquad (35)$$

$$\frac{\partial^2 \phi^{(m+1)}}{\partial \eta^2} + \frac{1}{\eta + k}\frac{\partial \phi^{(m+1)}}{\partial \eta} = -SrSc\left(\frac{\partial^2 \theta^{(m)}}{\partial \eta^2} + \frac{1}{(k + \eta)}\frac{\partial \theta^{(m)}}{\partial \eta}\right), \qquad (36)$$

$$\psi^{m+1} = -\frac{q}{2}, \ \frac{\partial \psi^{m+1}}{\partial \eta} = 1, \ \theta^{(m+1)} = 0, \ \phi^{(m+1)} = 0, \ \text{at } \eta = h_1, \quad (37)$$

$$\psi^{(m+1)} = \frac{q}{2}, \ \frac{\partial \psi^{(m+1)}}{\partial \eta} = 1, \ \theta^{(m+1)} = 1, \ \phi^{(m+1)} = 1, \ \text{at } \eta = h_2, \quad (38)$$

where the index (m) shows the iterative step.

In the next step, we insert the finite difference approximations of $\psi^{(m+1)}$, $\theta^{(m+1)}$, $\phi^{(m+1)}$, and their derivatives into Eqs. (34)–(36). In this way, we get a system of linear algebraic equations at each iterative step. These algebraic equations are solved at each cross section to get the numerical results of $\psi^{(m+1)}$, $\theta^{(m+1)}$, and $\phi^{(m+1)}$. For this purpose, appropriate initial guesses are required for $\psi^{(m)}$, $\theta^{(m)}$, and $\phi^{(m)}$ at each cross section to start the iterative procedure. For present computation, linear initial guesses (only satisfying the Dirichlet boundary conditions) are used. The iterative procedure at each cross section is carried out until a convergent solution is reached. The convergent solution is obtained rapidly by the method of successive under-relaxation. In this method, the values of $\tilde{\psi}^{(m+1)}$, $\tilde{\theta}^{(m+1)}$, and $\tilde{\phi}^{(m+1)}$ at the $(m + 1)$th iterative step are used to define convergent values $\psi^{(m+1)}$, $\theta^{(m+1)}$, and $\phi^{(m+1)}$ at the same step as follows:

$$\psi^{(m+1)} = \psi^{(m)} + \tau\left(\tilde{\psi}^{(m+1)} - \psi^{(m)}\right),$$
$$\theta^{(m+1)} = \theta^{(m)} + \tau\left(\tilde{\theta}^{(m+1)} - \theta^{(m)}\right), \qquad (39)$$
$$\phi^{(m+1)} = \phi^{(m)} + \tau\left(\tilde{\phi}^{(m+1)} - \phi^{(m)}\right),$$

where τ is the under relaxation parameter usually assumed small. Finally, in this way, the values of ψ, θ, and ϕ are achieved.

IV. COMPUTATIONAL RESULTS AND INTERPRETATION

The computations carried out using the aforementioned method are displayed in terms of velocity profiles, pressure rise per wavelength profiles, temperature and concentration profiles, and streamline contours. The truncation in the coefficient of heat transfer at the upper wall is also preceded.

The axial velocity profiles for some specific values of thermal Grashof number (Gr_T), concentration Grashof number (Gr_C), Hartmann number (Ha), and curvature parameter (γ), are shown in Figs. 2–5, respectively. Figure 2 shows an increase in the amplitude of the axial velocity with an increase in the thermal Grashof number. Thermal Grashof number is a parameter based on relative magnitudes of buoyancy and viscous forces. Larger values of Grashof number correspond to the situation in which buoyancy effects are dominant over the viscous effects. Now, due to the curvature in the channel, it is naturally anticipated that the flow velocity will be asymmetric for smaller values of thermal Grashof number, i.e., for weaker buoyancy effects. Figure 2 confirms the anticipated asymmetric profile for thermal Grashof number $Gr_T = 0$ with the
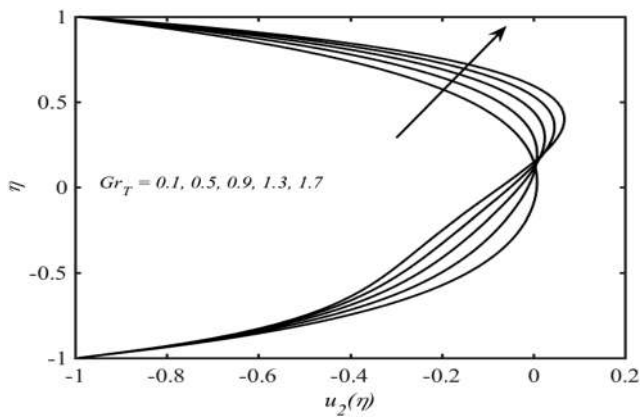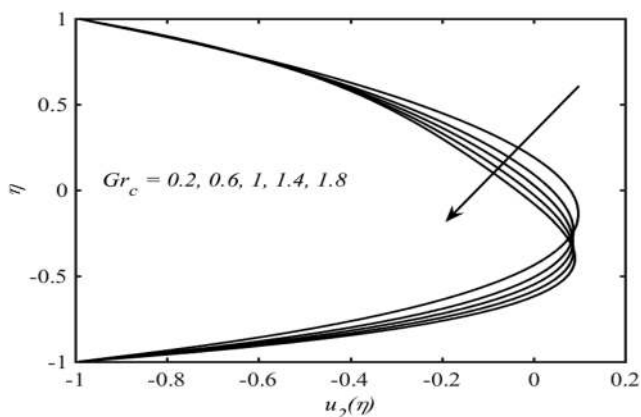
FIG. 2. $u_2(\eta)$ for various values of Gr_T with $\gamma = 2$, $Ha = 0.5$, $\lambda = 0.4$, $Gr_C = 2$, and $\Theta = 1.5$.
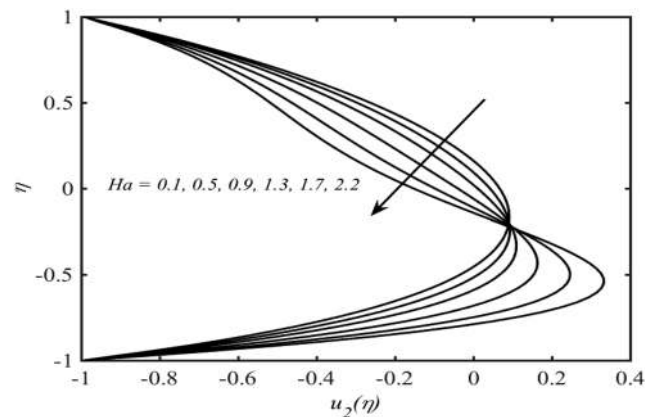

FIG. 4. $u_2(\eta)$ for various values of Ha with $\gamma = 2$, $Gr_T = 0.2$, $\lambda = 0.4$, $Gr_C = 2$, and $\Theta = 1.5$.

maximum lying below $\eta = 0$. For increasing values of Gr_T, the buoyancy effects dominate the viscous effects and shift the maxima in axial velocity profiles above $\eta = 0$. Therefore, it is concluded that Gr_T plays a valuable role in counteracting the influence of the curvature and facilitates the axial velocity to regain symmetry. This observation is quite interesting and it may find application in scenarios where it is desired to minimize the effects of the curvature without changing the geometry of the channel. This observation also highlights the role of the thermal field in tuning the transport process without altering the geometrical and rheological parameters of the model. The role of the rheological features of the fluid in tuning the transport in a curved channel is already highlighted by Bhatti *et al.*[29] Figure 3 presents the profiles of the axial velocity for several values of the concentration Grashof number Gr_C. The concentration Grashof number is a parameter based on relative magnitudes of the buoyancy force due to concentration gradients and the viscous force. Larger values of Gr_C correspond to the situation in which the buoyancy force due to concentration gradients is large.

Contrary to Figs. 2 and 3 shows that an increase in the concentration Grashof number shifts the maxima in the velocity profile toward the lower wall of the channel. In this way, an increase in the concentration Grashof number intensifies the effect of the curvature. The effects of the Hartmann number on the axial velocity are displayed in Fig. 4. The Hartmann number is a parameter number based on relative magnitudes of magnetic force and viscous force. Larger values of the Hartmann number correspond to the situation in which the magnetic force dominates the viscous force. It is observed that an increase in the Hartmann number suppresses the velocity in the upper part of the channel. The suppression is due to the fact that the Lorentz force due to the magnetic field acts as a resistance to the flow due to peristalsis. However, suppression in the axial velocity amplitude is not observed over the entire cross section. In fact, the velocity in the lower part of the channel increases with an increase in the Hartmann number in order to maintain the prescribed flow rate boundary condition. Figure 5 displays the effect of the dimensionless radius of the curvature parameter γ on the axial velocity. This figure

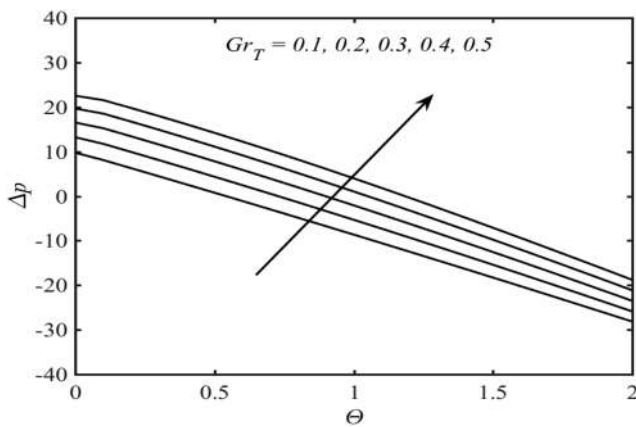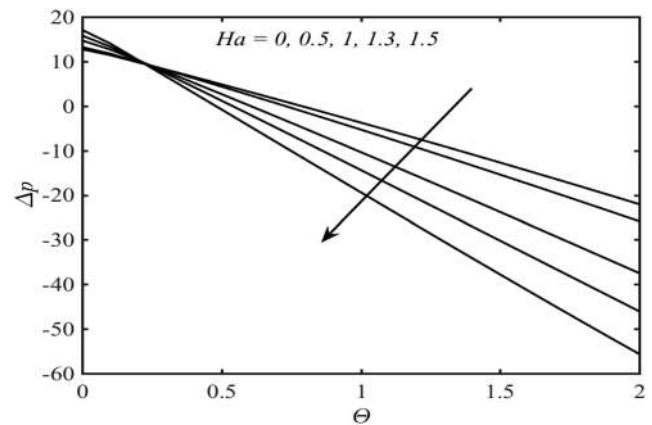**FIG. 3**. $u_2(\eta)$ for various values of Gr_C with $\gamma = 2$, $Ha = 0.5$, $\lambda = 0.4$, $Gr_T = 0.2$, and $\Theta = 1.5$.
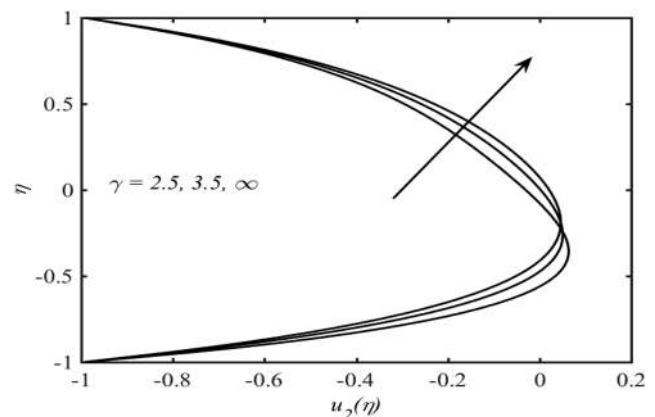
FIG. 5. $u_2(\eta)$ for various values of γ with $Gr_T = 0.2$, $Ha = 0.5$, $\lambda = 0.4$, $Gr_C = 2$, and $\Theta = 1.5$.

clearly demonstrates asymmetry in the axial velocity for decreasing values of γ.

Figures 6–9 demonstrate the effect of different parameters on the pressure rise per wavelength. Figure 6 depicts the effect of the thermal Grashof number Gr_T on Δp. It is noticed that the pressure rise per wavelength increases with an increase in Gr_T in all three regions, namely, peristaltic pumping region, free pumping region and co-pumping region. Figure 7 shows the effect of the concentration Grashof number Gr_C on Δp. A reverse trend is noted here, i.e., the pressure rise per wavelength decreases with an increase in Gr_C in all three regions. The profiles of the pressure rise per wavelength for different values of Ha (Hartmann number) are shown in Fig. 8. In the pumping region ($\Theta > 0$, $\Delta p > 0$), the pressure rise per wavelength increases with an increase in Ha. The situation is different in free pumping ($\Delta p = 0$) and co-pumping regions ($\Theta > 0$, $\Delta p < 0$). Here, Δp decreases with an increase in Ha.

FIG. 8. Δp for various values of Ha with $\gamma = 2$, $Gr_T = 0.2$, $\lambda = 0.4$, $Gr_C = 2$, and $\Theta = 1.5$.

FIG. 6. Δp for various values of Gr_T with $\gamma = 2$, $Ha = 0.5$, $\lambda = 0.4$, $Gr_C = 2$, and $\Theta = 1.5$.
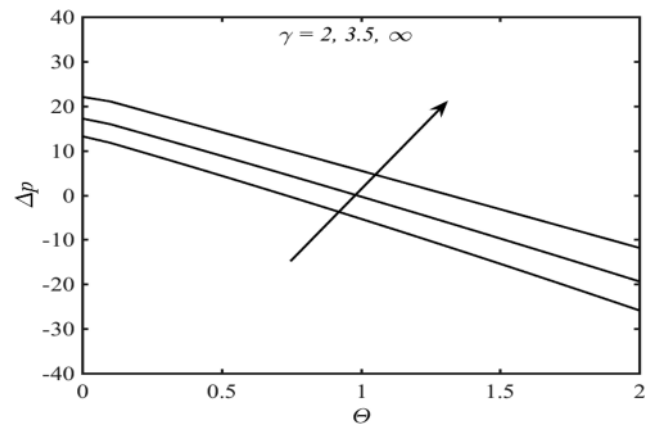

FIG. 9. Δp for various values of γ with $Gr_T = 0.2$, $Ha = 0.5$, $\lambda = 0.4$, $Gr_C = 2$, and $\Theta = 1.5$.

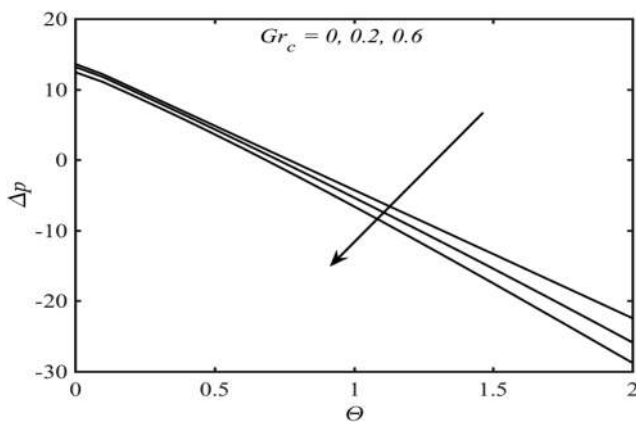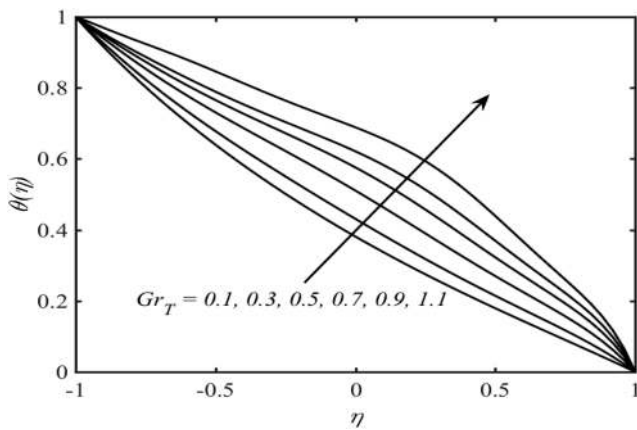**FIG. 7**. Δp for various values of Gr_C with $\gamma = 2$, $Ha = 0.5$, $\lambda = 0.4$, $Gr_T = 0.2$, and $\Theta = 1.5$.

Figure 9 depicts the effect of the non-dimensional radius of the curvature on Δp. It is observed that Δp increases with an increase in γ in all three regions. Both figures clearly highlight the significant effects of the buoyancy force, magnetic force, and curvature on Δp. In fact, the resistance offered by the pressure gradient to peristaltic flow can be minimized by suitable choice of the involved parameters.

The profiles of the temperature field for different values of the thermal Grashof number (Gr_T), Brinkman number (Br), and Hartmann number (Ha) are shown through Figs. 10–12. It is noted that $\theta(\eta)$ increases over the entire cross section with an increase in each of Gr_T, Br, and Ha. The increase in $\theta(\eta)$ with an increase in Gr_T and Ha is due to the retarding effect of these parameters on the velocity $u(\eta)$. The Brinkmann number is a parameter that is the ratio of viscous heat to the heat transported by conduction. Larger values of the Brinkmann number correspond to the scenario when heat
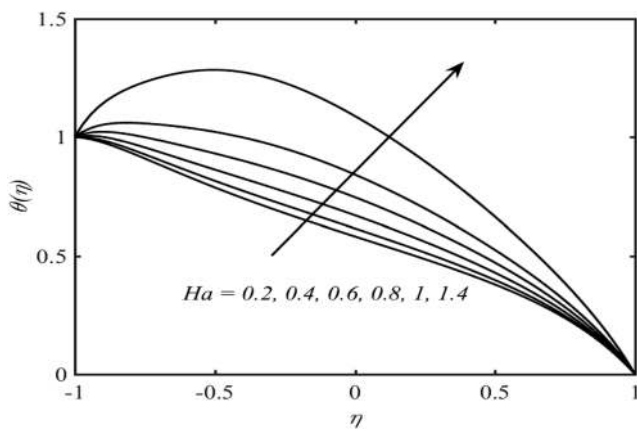
FIG. 10. $\theta(\eta)$ for various values of Gr_T with $\gamma = 2$, $Ha = 0.5$, $\lambda = 0.4$, $Br = 2$, and $\Theta = 1.5$.
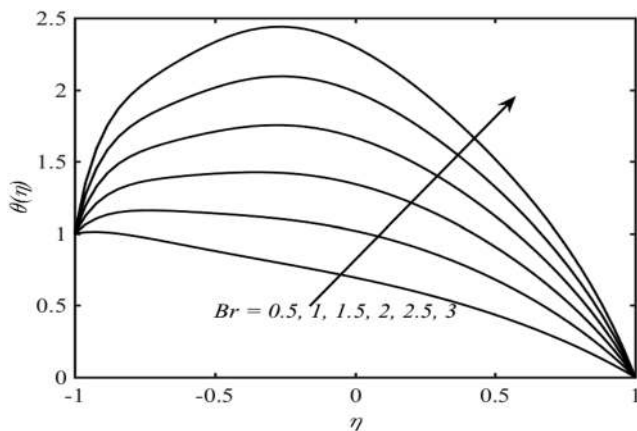
FIG. 11. $\theta(\eta)$ for various values of Br with $\gamma = 2$, $Ha = 0.5$, $\lambda = 0.4$, $Gr_T = 0.2$, and $\Theta = 1.5$.
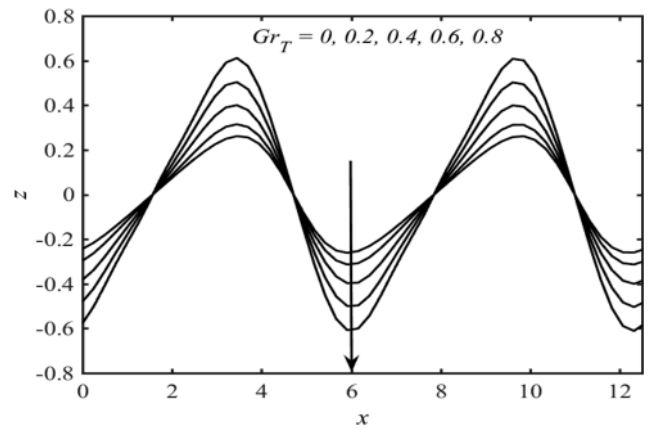

FIG. 12. $\theta(\eta)$ for various values of Ha with $\gamma = 2$, $Gr_T = 0.2$, $\lambda = 0.4$, $Br = 2$, and $\Theta = 1.5$.

generated due to viscous dissipation is dominant. In such a situation, the enhanced temperature distribution in the curved channel is apparently justified.

Figures 13–15 report changes in the heat transfer coefficient (z) at both walls of the channel with the variation of Gr_T, Br, and Ha. A periodic oscillation in the distribution of z has been noticed due to the fact that the walls of the channel are assumed to be oscillatory. Maximum values of these parameters enhance the amplitude of oscillations effectively.

The effect of Gr_T (thermal Grashof number), Br (Brinkman number), Ha (Hartmann number), and Gr_C (concentration Grashof number) on the mass transfer is demonstrated through Figs. 16–19. It is observed that $\phi(\eta)$ decreases with an increase in Gr_T, Br, and Ha, respectively. In contrast, the profile of $\phi(\eta)$ improves with leading values of Gr_C.
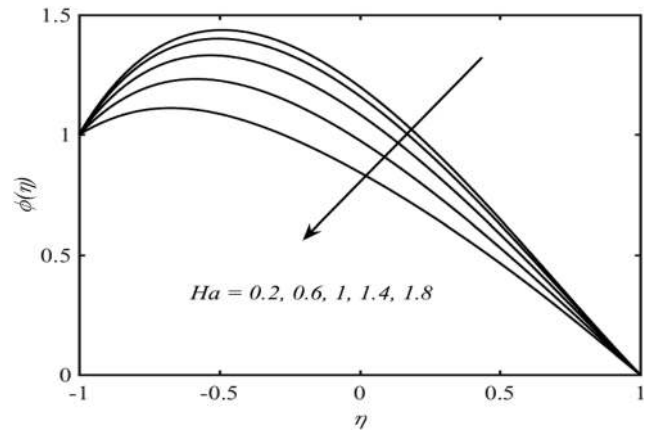

FIG. 13. z for various values of Gr_T with $\gamma = 2$, $Ha = 0.5$, $\lambda = 0.4$, $Br = 0.5$, and $\Theta = 1.5$.
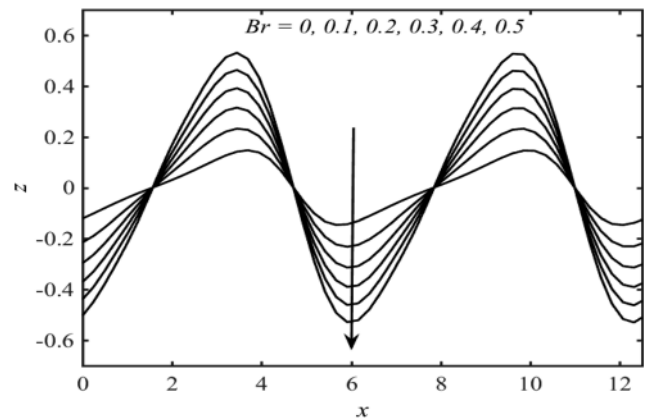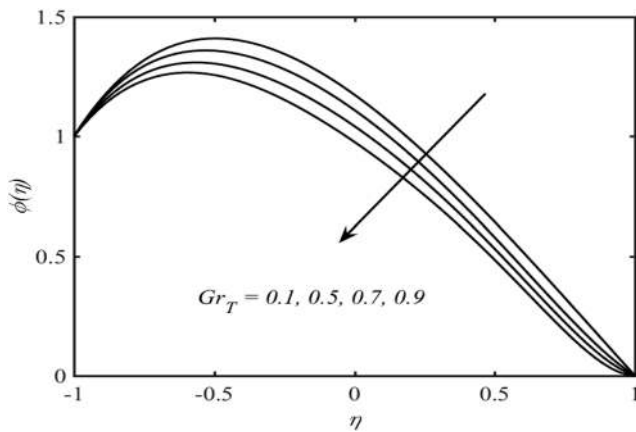

FIG. 14. z for various values of Br with $\gamma = 2$, $Ha = 0.5$, $\lambda = 0.4$, $Gr_T = 0.2$, and $\Theta = 1.5$.
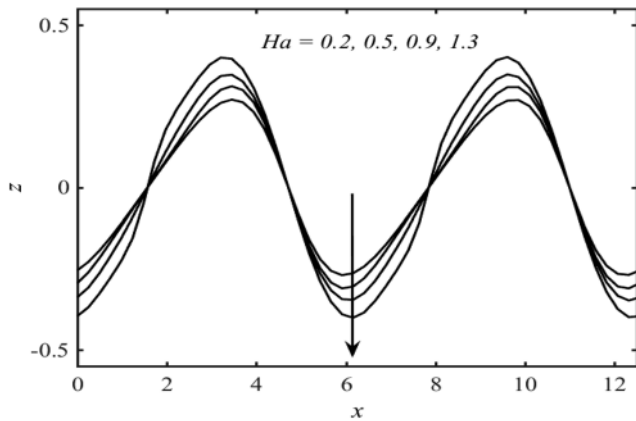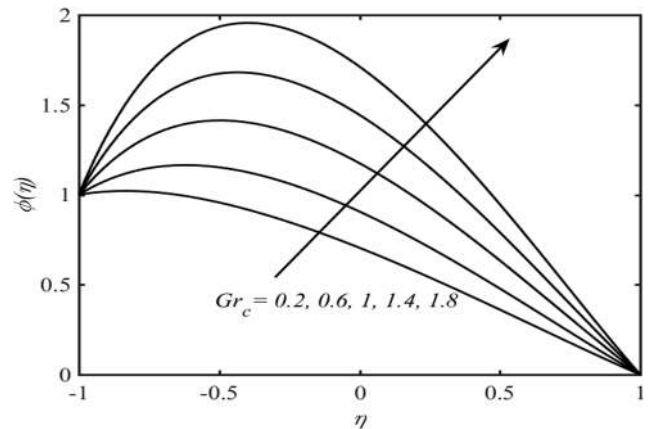
FIG. 15. z for various values of Ha with $\gamma = 2$, $Br = 0.5$, $\lambda = 0.4$, $Gr_T = 0.2$, and $\Theta = 1.5$.
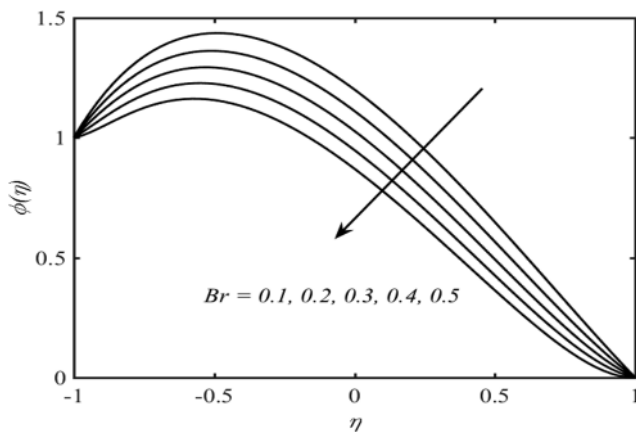

FIG. 18. $\phi(\eta)$ for various values of Ha with $\gamma = 2$, $Gr_T = 0.2$, $\lambda = 0.4$, $Sr = 1.5$, $Sc = 1.2$, and $\Theta = 1.5$.

FIG. 16. $\phi(\eta)$ for various values of Gr_T with $\gamma = 2$, $Br = 0.5$, $\lambda = 0.4$, $Sr = 1.5$, $Sc = 1.2$, and $\Theta = 1.5$.

FIG. 19. $\phi(\eta)$ for various values of Gr_C with $\gamma = 2$, $Gr_T = 0.2$, $\lambda = 0.4$, $Sr = 1.5$, $Sc = 1.2$, and $\Theta = 1.5$.

The streamlines of flow inside the channel for different values of Br (Brinkman number), Gr_T (Grashof number), and Ha (Hartmann number) are shown in Figs. 20–22. The objective is to investigate the trapping phenomenon. Figure 20 shows the effect of Br on streamlines. For $Br = 0.1$, two circulating rolls exist in the channel. The lower roll increases in size, while the upper one reduces with an increase in Br. The two circulating cells in the lower roll also merge into a single cell with an increase in Br. Figure 21 facilitates to examine the consequences of Gr_T on streamlines. Figure 21 shows a complex streamlines pattern with multiple circulating cells for $Gr_T = 0.1$. All these cells merge into a single circulating roll with an increase in Gr_T. Figure 22 portrays the effects of the Hartmann number on streamlines. For $Ha = 0.6$, two circulating rolls can be identified in the flow field. The upper one in the vicinity of the upper wall is smaller in size than the lower one. The inner most circulating cells in the lower roll splits into circulating cells with an increase in the Hartmann number.
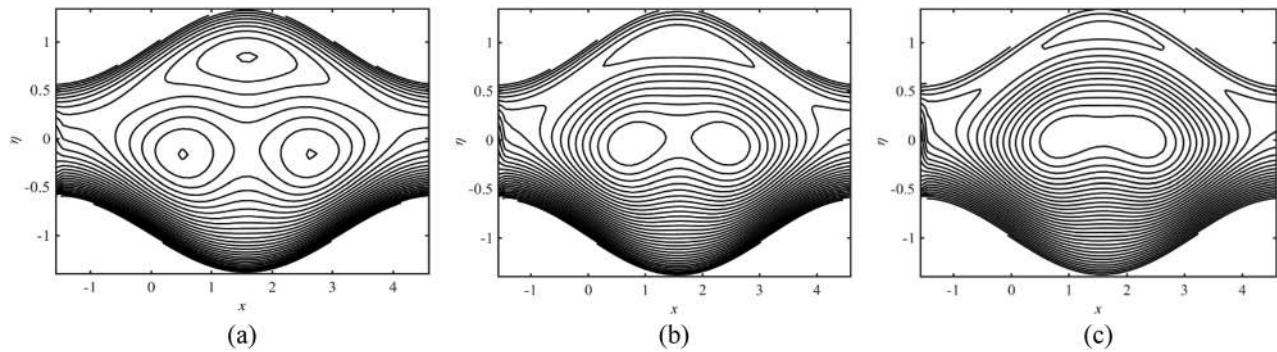

FIG. 17. $\phi(\eta)$ for various values of Br with $\gamma = 2$, $Gr_T = 0.2$, $\lambda = 0.4$, $Sr = 1.5$, $Sc = 1.2$, and $\Theta = 1.5$.

FIG. 20. Variation of Br for (a) 0.1, (b) 0.2, and (c) 0.3. The other parameters chosen are $\gamma = 2$, $Ha = 0.5$, $\lambda = 0.4$, $Gr_T = 0.2$, and $\Theta = 1.5$.
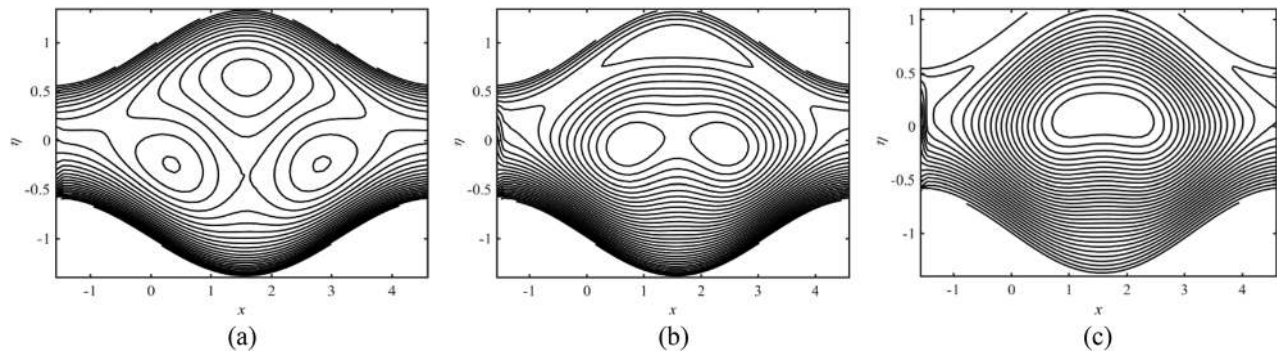

FIG. 21. Variation of Gr_T for (a) 0.1, (b) 0.2, and (c) 0.3. The other parameters chosen are $\gamma = 2$, $Ha = 0.5$, $\lambda = 0.4$, $Br = 2$, and $\Theta = 1.5$.
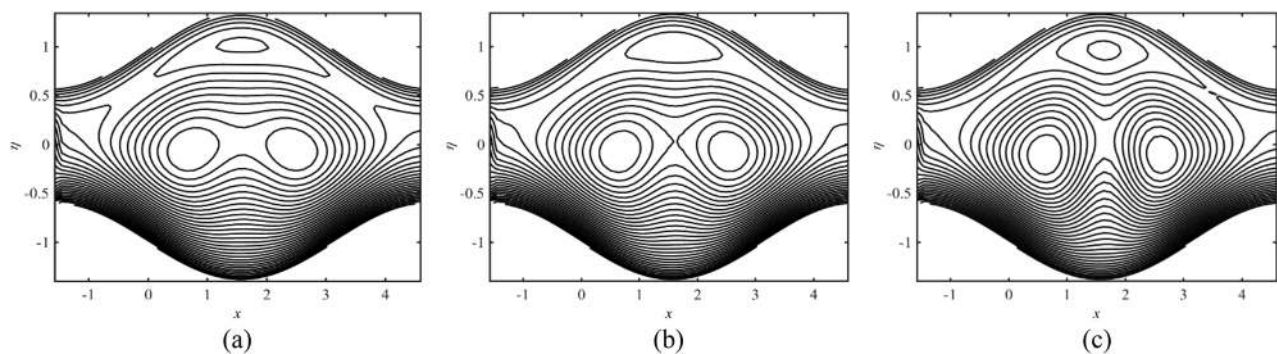

FIG. 22. Variation of Ha for (a) 0.6, (b) 1, and (c) 1.4. The other parameters chosen are $\gamma = 2$, $Gr_T = 0.2$, $\lambda = 0.4$, $Br = 2$, and $\Theta = 1.5$.

V. CONCLUDING REMARKS

We have performed heat and mass transfer analysis in the peristaltic transport of viscous fluid through a curved channel with an additional impact of mixed convection. The flow model is formulated under the assumptions of long wavelength. The numerical solution is computed via the finite difference algorithm and a detailed graphical analysis has been suggested with relevant physical features. The observations from current attempts are summarized in the following points:

- The flow velocity and pressure increase with the leading variation of the thermal transfer Grashof constant. However, the effectiveness of the Grashof number and Hartmann number on both profiles is quite the opposite.
- The temperature field is enhanced with an increase in the thermal Grashof number and Hartmann number.
- The mass concentration decreases with an increase in the thermal Grashof number and Hartmann number, while it increases with an increase in the concentration Grashof number.
- The circulations become intense for greater values of the Brinkman number, thermal Grashof number, and Hartmann number.
- Thus, more mixing is realized in mixed convective peristaltic flow than that in a purely peristaltic flow.

NOMENCLATURE

b	amplitude of wave m
c	wave speed m s^{-1}
c_p	specific heat at constant pressure m^2 s^{-2} K^{-1}
C	mass concentration kg
D	coefficient of mass diffusivity m^2 s^{-1}
k	thermal conductivity W m^{-1} K^{-1}
K_T	thermal diffusivity m^2 s^{-1}
T	temperature K
T_m	mean fluid temperature K
u_1, u_2	velocity component m s^{-1}
λ^*	wavelength m
μ	viscosity kg m^{-1} s^{-1}
ρ	density kg m^{-3}
Φ	dissipation function kg m^{-1} s^{-3}

DATA AVAILABILITY

The data that support the findings of this study are available within the article.

REFERENCES

[1]N. Ramachandran, T. S. Chen, and B. F. Armaly, "Mixed convection in stagnation flows adjacent to vertical surfaces," ASME J. Heat Transfer **110**, 373–377 (1998).

[2]A. J. Chamkha and C. Issa, "Mixed convection effects on unsteady flow and heat transfer over a stretched surface," Int. Commun. Heat Mass Transfer **26**, 717–727 (1999).

[3]Y. Y. Lok, N. Amin, D. Campean, and I. Pop, "Steady mixed convection flow of a micropolar fluid near the stagnation point on a vertical surface," Int. J. Numer. Methods Heat Fluid Flow **15**, 654–670 (2005).

[4]A. M. Rohni, S. Ahmad, I. Pop, and J. H. Merkin, "Unsteady mixed convection boundary layer flow with suction and temperature slip effects near the stagnation point on a vertical permeable surface embedded in a porous medium," Transp. Porous Media **92**, 1–14 (2012).

[5]Y. Y. Lok, I. Pop, D. B. Ingham, and N. Amin, "Mixed convection flow of a micropolar fluid near a non-orthogonal stagnation-point on a stretching vertical sheet," Int. J. Numer. Methods Heat Fluid Flow **19**, 459–483 (2008).

[6]K. V. Prasad, K. Vajravelu, and P. S. Datti, "Mixed convection heat transfer over a non-linear stretching surface with variable fluid properties," Int. J. Non Lin. Mech. **45**, 320–330 (2010).

[7]K. Bhattacharyya, S. Mukhopadhyay, and G. C. Layek, "MHD boundary layer slip flow and heat transfer over a flat plate," Chin. Phys. Lett. **28**, 024701 (2011).

[8]P. Rana, R. Bhargava, and O. A. Bég, "Numerical solution for mixed convection boundary layer flow of a nanofluid along an inclined plate embedded in a porous medium," Comput. Math. Appl. **64**, 2816–2832 (2012).

[9]H. Rosali, A. Ishak, R. Nazar, and I. Pop, "Mixed convection boundary layer flow past a vertical cone embedded in a porous medium subjected to a convective boundary condition," Propul. Power Res. **5**, 118–122 (2016).

[10]K. Vajravelu, K. V. Prasad, P. S. Datti, and B. T. Raju, "Convective flow, heat and mass transfer of Ostwald-de Waele fluid over a vertical stretching sheet," J. King Saud Univ. Eng. Sci. **29**, 57–67 (2017).

[11]A. Ishak, R. Nazar, N. M. Arifin, and I. Pop, "Dual solutions in mixed convection flow near a stagnation point on a vertical porous plate," Int. J. Therm. Sci. **47**, 417–422 (2008).

[12]Z. Abbas, Y. Wang, T. Hayat, and M. Oberlack, "Mixed convection in the stagnation-point flow of a Maxwell fluid towards a vertical stretching surface," Nonlinear Anal.: Real World Appl. **11**, 3218–3228 (2010).

[13]A. Jamaludin, R. Nazar, and I. Pop, "Three-dimensional mixed convection stagnation-point flow over a permeable vertical stretching/shrinking surface with a velocity slip," Chin. J. Phys. **55**, 1865–1882 (2017).

[14]C. H. Chen, "Combined effects of Joule heating and viscous dissipation on magnetohydrodynamic flow past a permeable, stretching surface with free convection and radiative heat transfer," ASME J. Heat Transfer **132**, 064503 (2010).

[15]M. Turkyilmazoglu, "The analytical solution of mixed convection heat transfer and fluid flow of a MHD viscoelastic fluid over a permeable stretching surface," Int. J. Mech. Sci. **77**, 263–268 (2013).

[16]O. Aydin and A. Kaya, "Mixed convection of a viscous dissipating fluid about a vertical flat plate," Appl. Math. Model. **31**, 843–853 (2007).

[17]K. Mahmood, M. Sajid, N. Ali, and T. Javed, "Magnetohydrodynamic mixed convection stagnation-point flow of a viscous fluid over a lubricated vertical surface," Ind. Lubr. Tribol. **69**, 527 (2017).

[18]M. M. Bhatti, M. Marin, A. Zeeshan, R. Ellahi, and S. I. Abdelsalam, "Swimming of motile gyrotactic microorganisms and movement of nanoparticles in blood flow through anisotropically tapered arteries," Front. Phys. **8**, 95 (2020).

[19]L. Zhang, M. B. Arain, M. M. Bhatti, A. Zeeshan, and H. Hal-Sulami, "Effects of magnetic Reynolds number on swimming of gyrotactic microorganisms between rotating circular plates filled with nanofluids," Appl. Math. Mech. **41**(4), 637–654 (2020).

[20]N. T. M. Eldabe, M. F. El-Sayed, A. Y. Ghaly, and H. M. Sayed, "Mixed convective heat and mass transfer in a non-Newtonian fluid at a peristaltic surface with temperature-dependent viscosity," Arch. Appl. Mech. **78**, 599–624 (2008).

[21]S. Srinivas, R. Gayathri, and M. Kothandapani, "Mixed convection heat and mass transfer in peristaltic flow an asymmetric channel with peristalsis," Commun. Nonlinear Sci. Numer. Simulat. **16**, 1845–1862 (2011).

[22]S. Srinivas and R. Muthuraj, "Effects of chemical reaction and space porosity on MHD mixed convective flow in a vertical asymmetric channel with peristalsis," Math. Comput. Model. **54**, 1213–1227 (2011).

[23]S. Noreen, "Mixed convection peristaltic flow with slip condition and induced magnetic field," Eur. Phys. J. Plus **129**, 33 (2014).

[24]S. A. Shehzad, F. M. Abbasi, T. Hayat, and F. Alsaadi, "MHD mixed convective peristaltic motion of nanofluid with Joule heating and thermophoresis effects," PloS One **9**(11), e111417 (2014).

[25]F. M. Abbasi, T. Hayat, B. Ahmad, and G. Q. Chen, "Slip effects on mixed convective peristaltic transport of copper–water nanofluid in an inclined channel," PloS One **9**, e105440 (2015).

[26]A. Tanveer, T. Hayat, A. Alsaedi, and B. Ahmad, "Mixed convective peristaltic flow of Sisko fluid in curved channel with homogeneous–heterogeneous reaction effects," J. Mol. Liq. **233**, 131–138 (2017).

[27]T. Hayat, S. Farooq, A. Alsaedi, and B. Ahmad, "Numerical analysis for radial MHD and mixed convection effects in peristalsis of non-Newtonian nanomaterial with zero mass flux conditions," Results Phys. **7**, 451–458 (2017).

[28] T. Hayat, F. M. Abbasi, B. Ahmad, and A. Alsaedi, "MHD mixed convection peristaltic flow with variable viscosity and thermal conductivity," Sains Malays **43**, 1583–1590 (2014).

[29] M. M. Bhatti, R. Ellahi, A. Zeeshan, M. Marin, and N. Ijaz, "Numerical study of heat transfer and Hall current impact on peristaltic propulsion of particle-fluid suspension with compliant wall properties," Mod. Phys. Lett. B **33**(35), 1950439 (2019).

[30] M. M. Bhatti, A. F. Elelamy, S. M. Sait, and R. Ellahi, "Hydrodynamics interactions of metachronal waves on particulate-liquid motion through a ciliated annulus: Application of bio-engineering in blood clotting and endoscopy," Symmetry **12**, 532 (2020).

[31] T. Hayat, F. M. Abbasi, M. Al-Yami, and S. Monaquel, "Slip and Joule heating effects in mixed convection peristaltic transport of nanofluid with Soret and Dufour effects," J. Mol. Liq. **194**, 93–99 (2014).

[32] A. Abbasi, I. Ahmad, N. Ali, and T. Hayat, "An analysis of peristaltic motion of compressible convected Maxwell fluid," AIP Adv. **6**, 015119 (2016).

[33] K. Javid, N. Ali, and M. Sajid, "Simultaneous effects of viscoelasticity and curvature on peristaltic flow through a curved channel," Meccanica **51**, 87–98 (2016).

[34] Z. Asghar and N. Ali, "Mixed convective heat transfer analysis for the peristaltic transport of viscoplastic fluid: Perturbation and numerical study," AIP Adv. **9**, 095001 (2019).